PTEP

Prog. Theor. Exp. Phys. **2023** 023I01(20 pages)
DOI: 10.1093/ptep/ptac164

Topological states in one-dimensional $\mathcal{PT}$-symmetric non-Hermitian spin-orbit-coupled Su–Schrieffer–Heeger lattices

Jia-Rui Li, Zi-An Wang, Tong-Tong Xu, Lian-Lian Zhang, and Wei-Jiang Gong*

College of Sciences, Northeastern University, Shenyang 110819, China.
*E-mail: gwj@mail.neu.edu.cn

Received August 29, 2022; Revised November 25, 2022; Accepted December 10, 2022; Published December 12, 2022

Energy and topological-state properties of the one-dimensional non-Hermitian spin-orbit-coupled Su–Schrieffer–Heeger lattice are theoretically investigated by introducing spin-dependent onsite imaginary potentials with gain and loss. It is found that imaginary potentials lead to the appearance of imaginary energies in the topologically nontrivial phase region, and $\mathcal{PT}$ phase transition occurs in the topologically trivial region. In addition, the imaginary potentials and spin–orbit coupling act together to make the topological phase transition occur in the topologically trivial region, and the topologically nontrivial region becomes wider. The energy spectrum results show that imaginary potentials and spin–orbit coupling have obvious effects on the zero-energy edge states of this system, which mainly lie in the presence of four types of zero-energy states with different localization and numbers. Furthermore, we discuss diagonal disorder and the transport behavior of system, further characterizing the properties of the individual topological states. The above results indicate the special adjustment effect of imaginary potentials and spin–orbit coupling on the band structure of such a system.

Subject Index I02

1. Introduction

In recent years, non-Hermitian Hamiltonians with combined inversion and time-reversal symmetries ($\mathcal{PT}$ symmetry) have been a research hotspot in the field of quantum and condensed-matter physics. The concept of $\mathcal{PT}$ symmetry was first proposed by Bender and Boettcher in 1998 [1]. They found that such a system is allowed to display the purely real eigenenergy spectrum before the occurrence of $\mathcal{PT}$ symmetry breaking. With the development of non-Hermitian and topological quantum physics, $\mathcal{PT}$-symmetric topological quantum physics has become an important research direction [2–9].

Among various geometries of non-Hermitian $\mathcal{PT}$-symmetric systems, the Su–Schrieffer–Heeger (SSH) lattice is one of the most basic and important systems [10–12]. The so-called one-dimensional (1D) SSH structure is a 1D two-band lattice with alternating hopping coefficients [13–16]. In the Hermitian case, the band gap can be closed and reopened at the boundary of its Brillouin zone by adjusting the ratio of intracell and intercell hopping coefficients. This precisely corresponds with the occurrence of a topological phase transition [17]. Under open boundary conditions, edge states have opportunities to appear at both ends of the system with their zero energy in the band gap of the topologically nontrivial region. Because of its clear

topological characteristics, the SSH model is also regarded as an important research object of non-Hermitian topological quantum physics. Zhu et al. pioneered this topic and studied the $\mathcal{PT}$-symmetric non-Hermitian SSH model with imaginary potentials at both ends of the model [18]. It has been found that when imaginary potentials are introduced, the topologically trivial and topologically nontrivial regions of the system show different characteristics. In the topologically trivial region, imaginary potentials will cause the system to exhibit the phase transition of spontaneous $\mathcal{PT}$ symmetry breaking. In the topologically nontrivial region, only the spontaneous $\mathcal{PT}$-symmetry-breaking phase can be observed. Subsequently, many research groups have devoted themselves to the study of the properties of $\mathcal{PT}$-symmetric non-Hermitian SSH chains, aiming at investigation spontaneous $\mathcal{PT}$ symmetry breaking, the topological phase, singular points, and topological edge states [19–26]. Moreover, various mechanisms have been taken into account, including the presence of next-nearest-neighboring coupling. Following the reported results, other complex structures have also been discussed, such as $\mathcal{PT}$-symmetric trimer lattices, the Kitaev model, hexagonal honeycomb lattices, etc. [6,27–32].

Although no special $\mathcal{PT}$-symmetric systems have been observed in nature, equivalent systems can be realized experimentally. For example, complex potentials with gain and loss can be obtained by using an optical waveguide channel [33], and $\mathcal{PT}$ symmetry can be achieved by employing an optical microcavity or a unidirectional stealth Bragg grating structure [34,35]. The development of $\mathcal{PT}$-symmetric optics and topological photonics has directly promoted the research of $\mathcal{PT}$-symmetric topological systems. In non-Hermitian photonic lattices, $\mathcal{PT}$ symmetry can also be achieved by nonlinearly tuning the loss of topological defect potential [36]. In addition to optical and photonic means, $\mathcal{PT}$ symmetry has been reported to be realizable in acoustics [37] and LRC circuits (L, R, and C represent the inductance, resistance, and capacitance of the circuit, respectively.) [38,39].

Following the in-depth study of spin–orbit-coupled systems, some research groups have highlighted that the spin–orbit coupling has an important influence and driving effect on the topological properties of Hermitian systems [40–42]. Inspired by this fact, our present work intends to design a complex system, that is, a 1D spin–orbit-coupled SSH lattice with spin-dependent imaginary potentials applied to the respective sites. Our purpose is to study the co-influence of imaginary potentials and spin–orbit coupling on the topological properties of the 1D spin–orbit-coupled SSH lattice. The calculation results show that spontaneous $\mathcal{PT}$-symmetry breaking occurs with the increase of imaginary potentials. Meanwhile, the interplay of imaginary potentials and spin–orbit coupling will induce the phase transition in the topologically trivial region, and widen the topologically nontrivial phase region. In this process, the two parameters also produce different zero-energy edge states in the topologically nontrivial region. Furthermore, we also observe the robustness of different types of edge states to disorder by introducing diagonal disorder. Finally, the properties of the respective topological states have been further described by investigating the transmission behaviors of the SSH lattice. All the phenomena show that the imaginary potentials and spin–orbit coupling have rich regulatory effects on the topological properties and edge state characteristics of the non-Hermitian spin–orbit-coupled SSH lattice.

The specific content of this paper is organized as follows. In Sect. II, we introduce the Hamiltonian of our considered system and calculate the eigenenergies in the momentum space. The symmetries and topological phase transition condition under periodic boundary conditions are also discussed. In Sect. III, the properties of energy spectra under the open boundary condi-

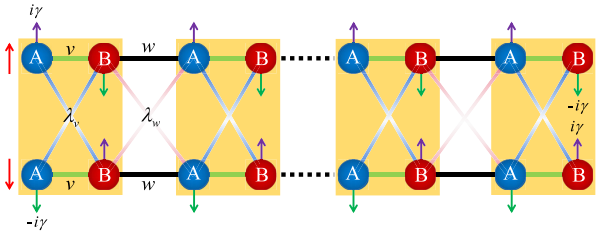

Fig. 1. Schematic diagram of the non-Hermitian spin–orbit SSH lattice. A and B represent two kinds of lattices; and purple up-arrows and green down-arrows represent imaginary potentials $i\gamma$ and $-i\gamma$, respectively. Light-green and black lines denote intracell hopping v and intercell hopping w, and the blue and pink lines describe the intracell spin–orbit coupling λ_v and the intercell spin–orbit coupling λ_w.

tion are explored, and we also discuss the diagonal disorder and transport behavior of system. Finally, Sect. IV provides a summary and concluding remarks.

2. Model and theory

The non-Hermitian 1D spin–orbit-coupled SSH lattice proposed in this work is composed of a 1D chain of N_c unit cells, as shown in Fig. 1. The Hamiltonian of the whole system is expressed as

$$H_c = H_0 + U. \tag{1}$$

The first term H_0 is the Hamiltonian of the 1D spin–orbit-coupled SSH lattice, that is,

$$\begin{aligned} H_0 = &\sum_{i=1}^{N_c}\sum_{\sigma}\left(v c_{ia\sigma}^{\dagger} c_{ib\sigma} + \text{h.c.}\right) + \sum_{i=1}^{N_c-1}\sum_{\sigma}\left(w c_{ib\sigma}^{\dagger} c_{i+1a\sigma} + \text{h.c.}\right) + \sum_{i=1}^{N_c}\sum_{\sigma\sigma'}\left(\lambda_v c_{ia\sigma}^{\dagger} c_{ib\sigma'} + \text{h.c.}\right) \\ &- \sum_{i=1}^{N_c-1}\sum_{\sigma\sigma'}\left(\lambda_w c_{ib\sigma}^{\dagger} c_{i+1a\sigma'} + \text{h.c.}\right). \end{aligned} \tag{2}$$

$c_{i\alpha\sigma}^{\dagger}$ and $c_{i\alpha\sigma}$ represent the creation and annihilation operators, respectively, with spin $\sigma(\sigma')[\sigma(\sigma') = \uparrow, \downarrow]$ on the αth ($\alpha = a, b$) lattice in the ith primitive cell. The h.c. represents the Hermitian conjugate. v refers to the intracell hopping, and its specific form is $v = t(1 + \delta)$. w denotes the amplitude of intercell hopping, defined as $w = t(1 - \delta)$. In order to ensure that all hopping terms are positive, this work defines the range of δ as $\delta < 1$. Next, $\lambda_v = \lambda(1 + \delta)$ and $\lambda_w = \lambda(1 - \delta)$ describe the spin–orbit coupling coefficients within and between protocells, respectively, where λ is the spin–orbit coupling strength.

In agreement with previous works, we would like to state that spin–orbit coupling can be realized in 1D cold atoms [43–45] and 1D photonic systems [46,47]. Experimental research teams have realized an orbital version of the SSH model by using the strong staggered hopping potential experienced by the doubly degenerate first-excited pillar modes, that is, p_x and p_y [47]. Whittaker et al. have experimentally explored the effect of photon spin–orbit coupling on topological side modes of SSH chains [46]. Therefore, it is plausible that our proposed spin–orbit-coupled SSH lattice can be realized experimentally.

The second term U describes the imaginary-potential terms realized by introducing energy gain and loss at the respective components of each site. Its Hamiltonian is written as

$$U = \sum_{i,\sigma} i\gamma\left(c_{ia\sigma}^{\dagger}\sigma_z^{\sigma\sigma} c_{ia\sigma} - c_{ib\sigma}^{\dagger}\sigma_z^{\sigma\sigma} c_{ib\sigma}\right), \tag{3}$$

in which $\gamma > 0$ denotes the imaginary-potential strength, and σ_z is the z component of the Pauli matrix.

The above Hamiltonian enables the band structure and topological properties of the non-Hermitian spin–orbit-coupled SSH system to be discussed in detail. Under a periodic boundary condition, one can obtain the Hamiltonian expression in the momentum space by performing the Fourier transformation $c_{i\alpha\sigma} = (1/\sqrt{N_c})\sum_k c_{k\alpha\sigma}e^{ikn}$, that is,

$$H_c = \sum_k \psi_k^\dagger H(k)\psi_k. \tag{4}$$

Consider the four component basis vector $\psi_k = [c_{ka\uparrow}, c_{ka\downarrow}, c_{kb\uparrow}, c_{kb\downarrow}]^{\mathrm{T}}$, $H(k)$ can be rewritten as

$$H(k) = \begin{bmatrix} i\gamma & 0 & z(k) & h(k) \\ 0 & -i\gamma & h(k) & z(k) \\ z^*(k) & h^*(k) & -i\gamma & 0 \\ h^*(k) & z^*(k) & 0 & i\gamma \end{bmatrix}, \tag{5}$$

in which k is the Bloch wave vector, $z(k) = v + we^{-ik}$, and $h(k) = \lambda_v - \lambda_w e^{-ik}$.

2.1 *Symmetry*

It is known that the symmetry of any Hamiltonian determines the symmetry-protected topological phase of the system with topological structure. Therefore, we should first pay attention to the system symmetry to present the topological properties of the spin–orbit-coupled SSH lattice. Using the Pauli matrices, Eq. (5) can be rewritten as

$$\begin{aligned} H(k) = {} & (v + \cos k)(\tau_x \otimes \sigma_0) + w \sin k(\tau_y \otimes \sigma_0) + (\lambda_v - \lambda_w \cos k)(\tau_x \otimes \sigma_x) \\ & - \lambda_w \sin k(\tau_y \otimes \sigma_x) + i\gamma(\tau_z \otimes \sigma_z). \end{aligned} \tag{6}$$

where $\tau_{x,y,z}(\sigma_{x,y,z})$ are the Pauli matrices in the corresponding subspaces, and $\tau_0(\sigma_0)$ are the related unit matrices.

In the case of $\gamma = 0$, the whole system is under the Hermitian condition. One can readily find that it satisfies the inversion symmetry $\mathcal{P}H(k)\mathcal{P}^{-1} = H(-k)$, and the operator $\mathcal{P}$ is expressed as $\tau_x \otimes \sigma_0$ ($\mathcal{P}^2 = 1$). The system also has time-reversal symmetry $\mathcal{T}H(k)\mathcal{T}^{-1} = H(-k)$, where $\mathcal{T} = (\tau_0 \otimes \sigma_x)\mathcal{K}$ ($\mathcal{T}\mathcal{T}^* = 1$), and $\mathcal{K}$ is expressed as complex conjugation. In addition, $H(k)$ satisfies the particle–hole symmetry $\mathcal{C}H(k)\mathcal{C}^{-1} = -H(-k)$, with Γ expressed as $\mathcal{C} = (\tau_z \otimes \sigma_0)\mathcal{K}$ and $\mathcal{C}\mathcal{C}^* = 1$. The existence of particle–hole symmetry ensures that the energy of our considered system satisfies positive and negative symmetries. Next, one can find that the system satisfies chiral symmetry $\Gamma H(k)\Gamma^{-1} = -H(k)$, in which Γ is expressed as $\Gamma = \tau_z \otimes \sigma_x$ ($\Gamma\Gamma^* = 1$).

On the other hand, in the case of $\gamma \neq 0$, the system becomes non-Hermitian. Since imaginary potentials give rise to $H \neq H^{\mathrm{T}}(H^*)$, the symmetry analysis on non-Hermitian systems will be changed in a substantial way. Kawabata et al. tried to give definitions and conditions for various symmetries of non-Hermitian systems [48]. They proposed that the definition of particle–hole symmetry (PHS) in the non-Hermitian case is $\mathcal{C}_- H^{\mathrm{T}}(k)\mathcal{C}_-^{-1} = -H(-k)$, and time-reversal symmetry (TRS) meets $\mathcal{T}_+ H^*(k)\mathcal{T}_+^{-1} = H(-k)$. In particular, in non-Hermitian systems, TRS† exists with $\mathcal{C}_+ H^{\mathrm{T}}(k)\mathcal{C}_+^{-1} = H(-k)$, and PHS† is manifested as $\mathcal{T}_- H^*(k)\mathcal{T}_-^{-1} = -H(-k)$. From the above symmetry expressions, it can be found that TRS† and PHS† are Hermitian conjugations of TRS and PHS, respectively.

Table 1. Symmetries satisfied by our systems in Hermitian and non-Hermitian cases.

Case	Symmetry	Definition	Operator
Hermitian	IS($\mathcal{P}$)	$\mathcal{P}H(k)\mathcal{P}^{-1} = H(-k)$	$\mathcal{P} = \tau_x \otimes \sigma_0$
	TRS($\mathcal{T}$)	$\mathcal{T}H(k)\mathcal{T}^{-1} = H(-k)$	$\mathcal{T}$=$(\tau_0 \otimes \sigma_x)\mathcal{K}$
	PHS($\mathcal{C}$)	$\mathcal{C}H(k)\mathcal{C}^{-1} = -H(-k)$	$\mathcal{C} = (\tau_z \otimes \sigma_0)\mathcal{K}$
	CS(Γ)	$\Gamma H(k)\Gamma^{-1} = -H(k)$	$\Gamma = \tau_z \otimes \sigma_x$
non-Hermitian	TRS†($\mathcal{C}_+$)	$\mathcal{C}_+ H^{\mathrm{T}}(k)\mathcal{C}_+^{-1} = H(-k)$	$\mathcal{C}_+ = \tau_0 \otimes \sigma_0$
	PHS†($\mathcal{T}_-$)	$\mathcal{T}_- H^*(k)\mathcal{T}_-^{-1} = -H(-k)$	$\mathcal{T}_- = \tau_z \otimes \sigma_0$
	CS(Γ)	$\Gamma H^\dagger(k)\Gamma^{-1} = -H(k)$	$\Gamma = \tau_z \otimes \sigma_0$
	$\mathcal{PT}$	$\mathcal{PT}H(k)\mathcal{PT}^{-1} = H(k)$	$\mathcal{P} = \tau_x \otimes \sigma_x$
			$\mathcal{T} = (\tau_0 \otimes \sigma_x)\mathcal{K}$

Table 2. The BDI and BDI† classes for Hermitian and non-Hermitian Hamiltonians.

Symmetry Class	TRS $\mathcal{T}(\mathcal{T}_+)$	PHS $\Gamma(\mathcal{C}_-)$	TRS† $\mathcal{C}_+$	PHS† $\mathcal{T}_-$	CS $\mathcal{C}$
BDI	+1	+1	0	0	1
BDI†	0	0	+1	+1	1

For our system, although TRS and PHS do not exist in the non-Hermitian case, $H(k)$ still satisfies the symmetries TRS† and PHS†, where the corresponding operators are $\mathcal{C}_+ = \tau_0 \otimes \sigma_0$ ($\mathcal{C}_+^2 = 1$) and $\mathcal{T}_- = \tau_z \otimes \sigma_0$ ($\mathcal{T}_-\mathcal{T}_-^* = 1$). Similarly, $H(k)$ satisfies chiral symmetry, that is, $\Gamma H^\dagger(k)\Gamma^{-1} = -H(k)$, where $\Gamma = \tau_z \otimes \sigma_0$. The chiral symmetry operator here can also be written as $\Gamma = \mathcal{C}_+\mathcal{T}_-$. In addition, the system satisfies $\mathcal{PT}$ symmetry, that is, $\mathcal{PT}H(k)\mathcal{PT}^{-1} = H(k)$, where $\mathcal{P}$ and $\mathcal{T}$ are respectively expressed as $\mathcal{P} = \tau_x \otimes \sigma_x$ and $\mathcal{T} = (\tau_0 \otimes \sigma_x)\mathcal{K}$. In Table 1, we summarize the symmetry of the system in both Hermitian and non-Hermitian cases.

Topological systems can be classified according to their symmetry [48,49]. It can be inferred that this system belongs to the BDI class in the Hermitian case, and belongs to the BDI† class in 38 topological classifications in the non-Hermitian case. The specific classification results are shown in Table 2. Previous conclusions show that there is a $\mathcal{Z}$-class topological invariant for 1D BDI-class systems [48]. Based on previous work [48,50], the topological phase transition condition of the BDI† class is determined by the band gap closing–reopening of the real part of energy bands. By calculating the det[$H(k)$], we find that the system satisfies the condition det[$H(k)$] $\neq 0$. In addition, the real part of the eigenvalues is not equal to zero except at the phase transition point. This result means the energy gap satisfies the real axis line gap L_r. According to the definition of complex-energy point (P) or line (L) gaps in the work of Kawabata [48], we can conclude that our system belongs to BDI† and can have a $\mathcal{Z}$-class topological invariant.

2.2 *Band structure and topological phase transition*

It should be understand that it is not accurate to determine the topological properties only from the perspective of symmetry. Therefore, the band structure of the 1D non-Hermitian spin–orbit-coupled SSH lattice is calculated to explore the topological phase transition conditions of our system. The energy-band expression in the momentum space can be obtained by

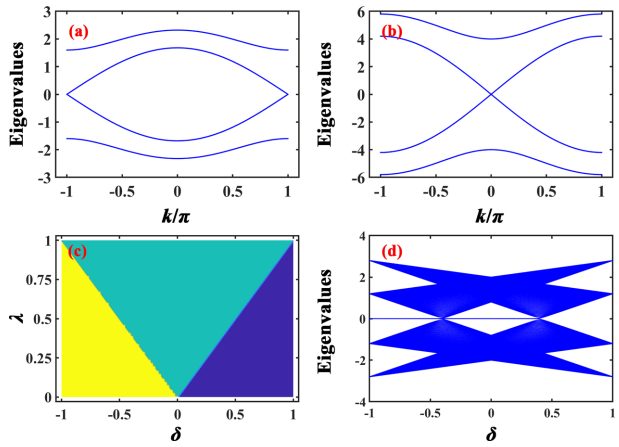

Fig. 2. (a,b) Energy spectra of the SSH system in the momentum space under the Hermitian condition with $\lambda = 0.4$. (a) and (b) show the results for $\delta = 0.4$ and $\delta = 2.5$, respectively. (c) Phase diagram in the momentum space, where the yellow region corresponds to $\mathcal{Z} = 2\pi$, the green region corresponds to $\mathcal{Z} = \pi$, and the purple region corresponds to $\mathcal{Z} = 0$. (d) Energy spectrum with the change of dimerization parameter δ.

diagonalizing the Hamiltonian of Eq. (5), that is,

$$E_{\pm}(k) = \pm\sqrt{X \pm \sqrt{-4\gamma^2|h(k)|^2 + Y}} \tag{7}$$

where

$$\begin{aligned} X &= -\gamma^2 + |h(k)|^2 + |z(k)|^2 \\ &= -\gamma^2 + \lambda_v^2 + \lambda_w^2 + v^2 + w^2 + 2(vw - \lambda_v\lambda_w)\cos k, \\ Y &= [h^*(k)z(k) + h(k)z^*(k)]^2 \\ &= 4[v\lambda_v - w\lambda_w + (w\lambda_v - v\lambda_w)\cos k]^2. \end{aligned} \tag{8}$$

For the Hermitian case ($\gamma = 0$), the eigenenergies in the momentum space are

$$E = \pm 2\sqrt{\left[(\lambda \pm t\delta)\sin\frac{k}{2}\right]^2 + \left[(t \pm \lambda\delta)\cos\frac{k}{2}\right]^2}. \tag{9}$$

Through the energy band expression, one can find that when $k = \pm\pi$, the middle two bands are closed. At this time, λ, δ, and t meet the condition $\delta = \pm\lambda/t$. Similarly, when the three parameters satisfy $\delta = \pm t/\lambda$, the middle bands will intersect at $k = 0$. For example, Fig. 2(a),(b) displays the energy spectra when $\lambda = 0.3$. It can be observed that when $\delta = 0.3$, the middle two bands intersect at $k = \pm\pi$, and when $\delta = 3.333$, the energy gap closes at $k = 0$, which is consistent with the theoretical derivation.

According to the conclusion of BDI-class symmetry, the system has $\mathcal{Z}$-class topological invariants. The Hamiltonian in the momentum space can be transformed into its off-diagonal form and substituted into the expression of topological invariant. Thus, we have

$$\mathcal{Z} = -\mathrm{Tr}\int_{-\pi}^{\pi}\frac{dk}{2i}V^{-1}\partial_k V = -\int_{-\pi}^{\pi}\frac{dk}{2i}\partial_k \ln\det(V), \tag{10}$$

in which V is expressed as

$$V = \begin{bmatrix} z(k) & h(k) \\ h(k) & z(k) \end{bmatrix} = \begin{bmatrix} v + we^{-ik} & \lambda_v - \lambda_w e^{-ik} \\ \lambda_v - \lambda_w e^{-ik} & v + we^{-ik} \end{bmatrix}.$$

Thus, $\det(V) = -\lambda_v^2 + v^2 + 2e^{-ik}(\lambda_v\lambda_w + vw) + e^{-2ik}(-\lambda_w^2 + w^2)$. Based on this formula, we can obtain the topological invariants in the Hermitian case. The corresponding results are shown in Fig. 2(c). It can be observed from the figure that when $\lambda = 0$, the system has only two phases, $\mathcal{Z} = 2\pi$ (yellow region) and $\mathcal{Z} = 0$ (purple region). With the increase of λ, the region within $-\lambda/t < \delta < \lambda/t$ is topologically nontrivial region I (green region). The results show that the presence of λ results in three phases, that is, $\mathcal{Z} = 2\pi$, $\mathcal{Z} = \pi$, and $\mathcal{Z} = 0$, in our system. Figure 2(d) shows the band structure under open boundary conditions. From previous research [40–42], it is known that when $\mathcal{Z} = 2\pi$, the zero modes have fourfold degeneracy, while when $\mathcal{Z} = \pi$, they change to exhibit twofold degeneracy. Therefore, the functions of spin–orbit coupling are: (i) improving the degeneracy of the system, (ii) producing the topological phase transition, (iii) and enriching the type of zero-energy states.

At the non-Hermitian case ($\gamma \neq 0$), the gap-closure condition can also be found from Eq. (7), and the expressions of the four bands of the system at $k = \pm\pi$ can be written as $E_{1(2)} = 2\lambda + (-)\sqrt{-\gamma^2 + 4\delta^2 t^2}$ and $E_{3(4)} = -2\lambda - (+)\sqrt{-\gamma^2 + 4\delta^2 t^2}$. According to the energy band expressions, if the two energy bands E_2 and E_3 intersect, we will have

$$\gamma^2 = 4(\delta^2 t^2 - \lambda^2). \tag{11}$$

When $k = 0$, the band expressions of the system become $E_{1(2)} = 2\lambda\delta + (-)\sqrt{-\gamma^2 + 4t^2}$ and $E_{3(4)} = -2\lambda\delta - (+)\sqrt{-\gamma^2 + 4t^2}$. E_2 and E_3 can also intersect at $k = 0$. At this time, all parameters must meet

$$\gamma^2 = 4(t^2 - \delta^2\lambda^2). \tag{12}$$

In addition, it can be found through the band expressions of $k = \pm\pi$ and $k = 0$ that if E_1 and E_2 (E_3 and E_4) intersect at these two locations, the parameters must meet $\gamma^2 = 4\delta^2 t^2$ and $\gamma^2 = 4t^2$.

Similar to the Hermitian case, to better observe the topological properties in the non-Hermitian case, we need to discuss the global Zak phase [51,52] in the momentum space. Note that in such a case, we have to use the original expression of the Zak phase, that is,

$$\mathcal{Z}' = \sum_{n=1}^{4} -\frac{1}{2i}\oint \langle\varphi_n|\partial_k\psi_n\rangle \mathrm{d}k, \tag{13}$$

because of the difficulty in the analytical derivation. Here, $|\psi_n\rangle(|\varphi_n\rangle)$ represents the right (left) vector eigenstate and satisfies $H_k|\psi_n\rangle = E_n|\psi_n\rangle$ and $h_k^\dagger|\varphi_n\rangle = E_n^*|\varphi_n\rangle$, and n is the band index [51–54]. By calculating the Zak phase $\mathcal{Z}'$, the topological phase region of the system can be identified. Figure 3 shows the topological phase diagram with the change of γ and λ when $\delta = 0.3$. The green region in the figure corresponds to the topologically nontrivial phase of $\mathcal{Z}' = \pi$, and the blue part represents the topologically trivial phase of $\mathcal{Z}' = 0$. It is obvious in the figure that under the condition of $0 < \lambda < \delta$, γ and λ can drive this system to undergo topological phase transition, resulting in the emergence of new topological phases.

According to the reports in previous works [51,52,55], the topologies can also be characterized by the geometry of the Bloch Hamiltonian winding around a degenerate point in the two-dimensional parameter space. Therefore, we also demonstrate the regulatory effect of imaginary potentials on the topological properties of our system. We replace e^{ik} of the Hamiltonian

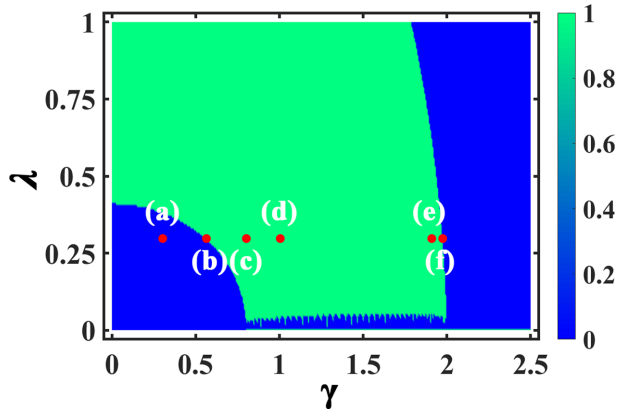

Fig. 3. Topological phase diagram with the change of γ and λ. The blue region corresponds to the topologically non-trivial phase of $\mathcal{Z}' = \pi$, and green region represents the topologically trivial phase of $\mathcal{Z}' = 0$. Relevant parameters are taken to be $\delta = 0.4$ and $t = 1.0$.

in the momentum space [see Eq. (5)] with $h_x + ih_y$. Accordingly,

$$H(k) = \begin{bmatrix} i\gamma & 0 & v + w(h_x - ih_y) & \lambda_v - \lambda_w(h_x - ih_y) \\ 0 & -i\gamma & \lambda_v - \lambda_w(h_x - ih_y) & v + w(h_x - ih_y) \\ v + w(h_x + ih_y) & \lambda_v - \lambda_w(h_x + ih_y) & -i\gamma & 0 \\ \lambda_v - \lambda_w(h_x + ih_y) & v + w(h_x + ih_y) & 0 & i\gamma \end{bmatrix}. \tag{14}$$

We set a unit circle $h_x^2 + h_y^2 = 1$ in the two-dimensional parameter space (h_x, h_y), which represents the momentum space Hamiltonian. Since the Dirac point appears at $\mathrm{Im}(E) = 0$, we can omit the imaginary σ_y term by taking $h_y = 0$.

Figure 4 shows the Hamiltonian structure extended to the two-dimensional parameter space (h_x, h_y) at fixed parameters $\lambda = 0.3$, $\delta = 0.4$, and $t = 1.0$ for the different imaginary potentials. The red cross represents the degenerate point (DP), whereas the blue cross represents the exceptional points (EPs). For $\gamma = 0$ in Fig. 4(a), the DP moves to the point $(-1.256, 0)$, and it is out of the winding. Hence, the system is located in the topologically trivial region. As γ increases, the DP gradually moves closer to the unit circle, as shown in Fig. 4(b),(c). In the critical case where $\gamma = \sqrt{7}/5$, the DP shifts to $(-1.0, 0)$ and is located on the unit circle. This means that the system reaches the critical position of the topological phase transition. When γ increases to 0.8 [see Fig. 4(d)], the EP appears on the boundary of the unit circle, and the DP enters the unit circle at this time. With the further increase of γ, the EP splits into two, showing the symmetric distribution of $h_y = 0$. Meanwhile, the DP gradually moves closer to (1.0, 0) as γ increases, and arrives at the unit circle boundary when $\gamma = 1.986$ [see Fig. 4(e),(f)]. During the whole change process from (–1.0,0) to (1.0,0), the system has been in the topologically non-trivial region. When $\gamma > 1.986$, the DP falls outside the unit circle, which indicates that the system is transformed from the topologically nontrivial to the topologically trivial phase. Two EPs merge into a single EP at $(h_x, h_y) = (1,0)$, and when $\gamma > 2.0$, the EP disappears. Therefore, the topological nature is fully determined by the central DP (red cross).

To better understand the results of DP and EP in the spectra of Fig. 4, we present the corresponding theoretical calculation. First, from Eq. (5) we can calculate the condition for the

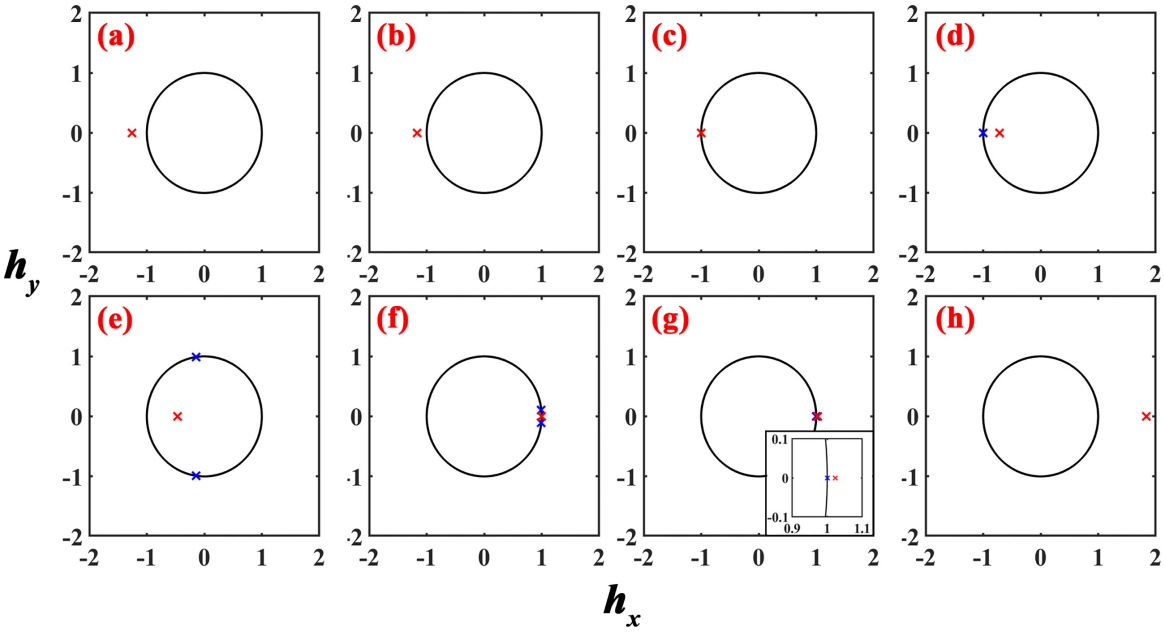

Fig. 4. (a)–(h) Geometric spectra of the topology in the two-dimensional parameter space (h_x, h_y) for one-dimensional $\mathcal{PT}$-symmetric non-Hermitian spin–orbit-coupled SSH lattice. The parameters are set as (a) $\gamma = 0$, (b) $\gamma = 0.3$, (c) $\gamma = \sqrt{7}/5$, (d) $\gamma = 0.8$, (e) $\gamma = 1.0$, (f) $\gamma = 1.986$, (g) $\gamma = 2$, and (h) $\gamma = 2.5$. The other parameters are $\delta = 0.4$, $\lambda = 0.3$, and $t = 1$.

appearance of EPs, that is,

$$k = \arccos\left[\frac{8\delta^2 t^2 - \gamma^2(1+\delta^2))}{\gamma^2(\delta^2-1)}\right]. \tag{15}$$

Following this condition, we can get the expression of EP in the (h_x, h_y) space. For the DPs, from the figures we find that they all appear at $h_y = 0$. Hence by diagonalizing the Hamiltonian in Eq. (13), we get

$$E_\pm = \pm[\lambda_v - h_x\lambda_w \pm \sqrt{-\gamma^2 + (v + h_x w)^2}]. \tag{16}$$

The resultant condition for degeneracy is given by $(\lambda_v - h_x\lambda_w)^2 = -\gamma^2 + (v + h_x w)^2$. After derivation, we get the corresponding expression for h_x, that is,

$$h_x = -\frac{wv + \lambda_v\lambda_w}{w^2 - \lambda_w^2} + \sqrt{\frac{\lambda_v^2 - v^2 + \gamma^2}{w^2 - \lambda_w^2} + \frac{(wv + \lambda_v\lambda_w)^2}{(w^2 - \lambda_w^2)^2}}. \tag{17}$$

Thus the degenerate zero points can be displaced to be $(h_x, h_y) = (h_x, 0)$. Through calculation, it can be concluded that the results derived above are consistent with the results in Fig. 4.

Following the above theoretical derivation, in Fig. 5 we present the eigenenergy spectra of the non-Hermitian 1D spin–orbit-coupled SSH model in the momentum space. Relevant parameters are set to $\lambda = 0.3$ and $\delta = 0.4$, corresponding to the topologically trivial region in the Hermitian case. It can be seen from the figure that with the increase of γ, the system has indeed experienced two phase transitions, which means that the imaginary potentials play an important role in regulating the topological properties of the system. Specifically, from Fig 5(a),(b) it can be observed that when γ increases to $\sqrt{7}/5$, the middle two bands meet at $k = \pm\pi$. During this process, the topological phase transition occurs, which is consistent with the result of Eq. (11). As γ continues to increase, the closed gap reopens when $\gamma = 0.8$ [as shown in Fig. 5(c)], the upper and lower bands intersect at $k = \pm\pi$, and the degenerate point is $|E| = 2\lambda$. When $\gamma > 2\delta t$,

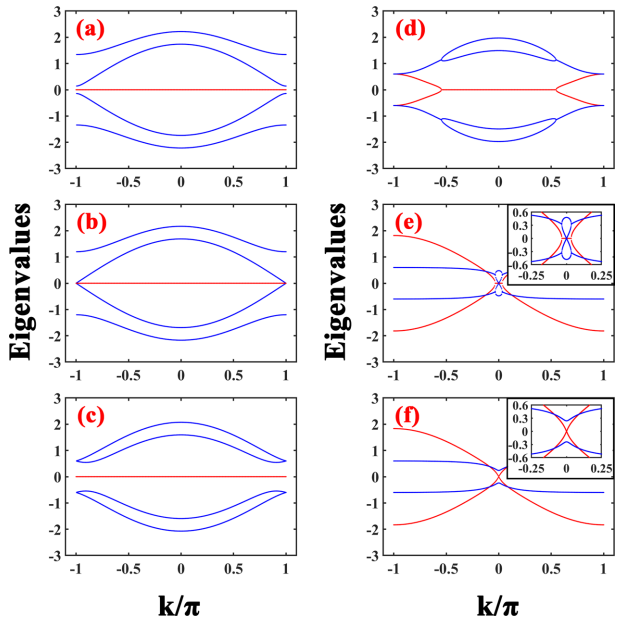

Fig. 5. Band structures for different values of imaginary potential γ. The value of γ is set to be (a) $\gamma = 0.3$, (b) $\gamma = \sqrt{7}/5$, (c) $\gamma = 0.8$, (d) $\gamma = 1.0$, (e) $\gamma \approx 1.986$, and (f) $\gamma = 2.0$, which correspond to the respective points in Fig. 3. The blue lines indicate the real part of energy, and the red lines correspond to the imaginary part. Other parameters are $\lambda = 0.3$ and $\delta = 0.4$.

the imaginary potentials split the degenerate point into two singular points related to the $\mathcal{PT}$ symmetry breaking. When $\gamma \approx 1.986$, the energy gap is closed again at $k = 0$, and the imaginary part of energy $\mathrm{Im}(E) = 0$ [as shown in Fig. 5(e)]. This shows that the system has a second phase transition, and the conditions are consistent with Eq. (12). With the increase of non-Hermitian potentials, the two singular points continue to move, and the complex energy region gradually extends to the center. When $\gamma = 2t = 2.0$, the two singular points merge at $k = 0$ and the imaginary part forms a Dirac cone at $k = 0$. At this time, the real part of the energy is $E = \pm 2\delta\lambda$ [as shown in Fig. 5(f)]. Finally, when $\gamma > 2t$, the energy of the whole system is complex and there is no singularity. Based on the above results, it can be determined that the imaginary potentials induce abundant band structures in the non-Hermitian spin–orbit-coupled SSH lattice.

3. Results and discussions

Based on the above results for the momentum space, we proceed to numerically discuss the band structure of the non-Hermitian 1D spin–orbit-coupled SSH lattice in detail under the open boundary condition. The order of discussion under the open boundary condition is as follows. First, we plot the energy spectra and observe the characteristics of the band structure. From the energy and probability density spectra, the localization of various edge states is discussed. Then, we focus on the effects of imaginary potentials and spin–orbit coupling strength, respectively. Next, we introduce two different mechanisms of diagonal disorders to observe the robustness of the edge states. Finally, we study the transmission properties by applying two semi-infinite lattices. For convenience, in the context we take $t = 1.0$ to perform the calculations.

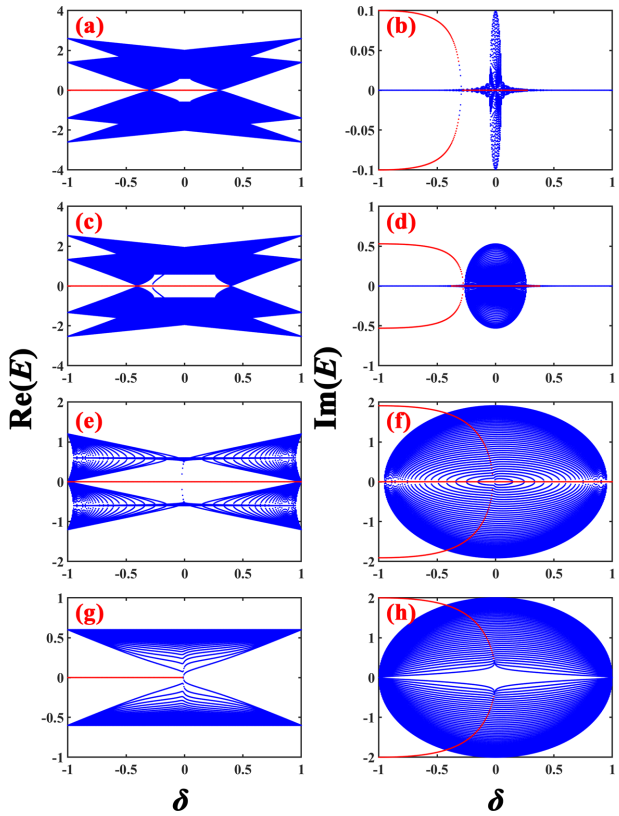

Fig. 6. Real and imaginary parts of energy for different δ. The parameters are (a),(b) $\gamma = 0.1$, (c),(d) $\gamma = \sqrt{7}/5$, (e),(f) $\gamma \approx 1.908$, and (g),(h) $\gamma = 2.0$. The left panels show the real part of energy, and the right panels correspond to the imaginary part of energy. Other parameters are $\lambda = 0.3$. The red lines denote the real and imaginary parts of zero-energy states.

3.1 *Appearance of edge states*

To begin with, we discuss the energy band structure of the system under the open boundary condition by setting $\lambda = 0.3$. According to the conclusion of the Hermitian case, when $\delta \in [-1.0, -0.3]$, there exist fourfold-degenerate zero-energy states, whereas if $\delta \in [-0.3, 0.3]$, twofold-degenerate zero-energy states emerge. The other region where $\delta \in [0.3, 1.0]$ is topologically trivial.

Figure 6 plots the real and imaginary parts of energy bands under the condition of $N_c = 50$. It can be seen from Eqs. (11) and (12) that in the non-Hermitian case, phase transition occurs at $\delta_{1(2)} = +(-)\sqrt{(\gamma^2 + 4\lambda^2)/4t^2}$ and $\delta_{3(4)} = +(-)\sqrt{(-\gamma^2 + 4t^2)/4\lambda^2}$. From the spectra of the real and imaginary parts of energy, it can be found that the imaginary potentials have different regulatory effects on the bulk states and zero-energy states of the topologically nontrivial and topologically trivial phases of our system. First, in the topologically trivial region (Hermitian case $0.3 < \delta < 1$), with the increase of γ, the zero-energy region induced by the imaginary potentials gradually widens. When $\gamma = 1.908$, the topological phase transition condition δ_1 is reached, and there is a zero-energy state in the whole region of $\delta \in [0.3, 1.0]$ [as shown in Fig. 6(e)]. There is no imaginary part in the new zero-energy state. In the topologically nontrivial region (Hermitian case $\delta \in [-1.0, 0.3]$), the effects of imaginary potentials on the two topologically nontrivial phases are different. The imaginary potentials lead to the finite imaginary part of the original fourfold-degenerate zero-energy states, that is, $E = 0 \pm ib$.

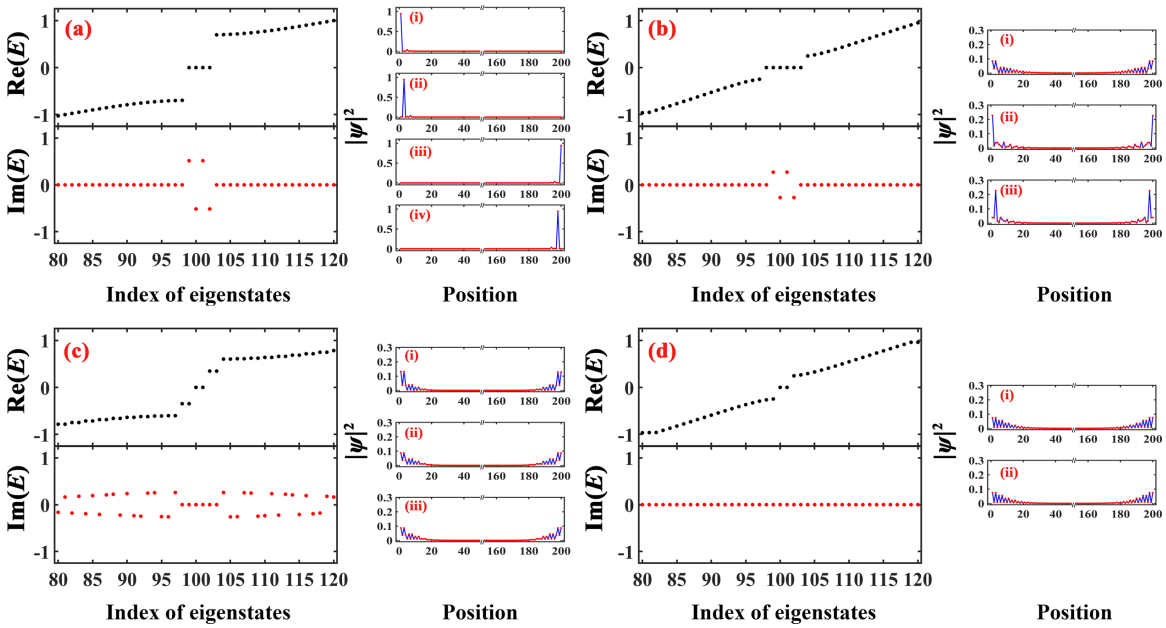

Fig. 7. Energy and probability density spectra under open boundary conditions, where (a) $\delta = -0.7$, (b) $\delta = -0.32$, (c) $\delta = -0.23$, and (d) $\delta = 0.32$. The other parameters are $\lambda = 0.3$ and $\gamma = \sqrt{7}/5$.

This indicates that the $\mathcal{PT}$-symmetry breaking occurs at this stage, while the original twofold-degenerate states still show their zero energy. The increase of γ makes the topological phase transition point that satisfies δ_2 gradually approach $\delta = -1.0$, resulting in the reduction of the region of original fourfold-degenerate zero-energy states and the gradual increase of the region of twofold zero-energy states. In addition, other isolated states separated from the bulk states appear in $\delta \in [-\delta_2, 0]$. As δ approaches -1.0, the isolated states also gradually change to be zero-energy with a finite imaginary part of the energy. Then, new region forms in which the states contain some purely real zero energy and some purely imaginary energies. Since the zero-energy states of this part are not caused by the closure and reopening of the band gap, it is inferred that they are not of a topological nature. When $\gamma = 2.0$, the breaking of the topological phase transition leads to the absence of a topological phase and the existence of only energy states with imaginary potential energy. For the bulk states, imaginary parts appear in the range of $-\gamma/2 < \delta < \gamma/2$ and $\mathcal{PT}$-symmetry breaking occurs, while the bulk states in other regions are real. Taking Fig. 6(g),(h) as an example, when $\gamma = 2.0$, the bulk states of the entire parameter space have imaginary parts. Based on the above results, it can be found that the imaginary potentials have an obvious regulatory effect on the band structure and topological states under open boundary conditions.

Fig. 7(a)–(d) shows the eigenenergy spectra and wavefunction probability density at $\delta = -0.7$, $\delta = -0.32$, $\delta = -0.23$, and $\delta = 0.32$, respectively. It can be observed that the zero-energy states in different regions show different characteristics. Specifically, when $\delta = -0.7$, there are four purely imaginary states in the band gap. In the probability density spectrum of Fig. 7(a), (i) and (iii) correspond to $0 + 0.514i$, respectively, (ii) and (iv) correspond to $0 - 0.514i$. Due to the presence of imaginary potentials, the eigenenergies become complex, the four states are localized at the left or right ends of the lattice, and the localization of the two states with the same energy are opposite. Figure 7(b) corresponds to the result for $\delta = -0.32$. It can be seen that there are six states in the band gap, four of which have imaginary energies and two of which are

purely real. It can be seen from the previous results that the states with imaginary energies are caused by the isolated states precipitated from the bulk states, and do not have topology. From the probability density, it can be found that two purely real zero-energy states (i) are localized at both ends of the system. The four states with energies of $0 + 0.271i$ (ii) and $0 - 0.271i$ (iii) also tend to be localized at both ends of the system. In order to determine the isolated state precipitated from the system, Fig. 7(c) shows the result for $\delta = -0.23$. It can be observed from the energy spectrum that the newly generated isolated state is twofold degenerate, and purely-real twofold-degenerate zero-energy states are formed in the middle of the band gap. From the probability density, it can be seen that the isolated states and the zero-energy states are localized at both ends of the system. However, compared with the zero-energy mode generated by the isolated states [Fig. 7(b) (ii) and (iii)], the localization is relatively weak. Finally, when $\gamma = 0.32$, the imaginary potentials cause the twofold-degenerate zero-energy states localized at both ends of the system to appear in the gap of the original topologically trivial region, as shown in Fig. 7(d). To sum up, the addition of imaginary potentials leads to the appearance of twofold-degenerate zero-energy states localized at both ends of the system in the gap of the original topologically trivial region. With the precipitation of the twofold-degenerate isolated states into the zero-energy states, the original twofold real zero-energy states become six states. This suggests that the imaginary potentials can make the zero-energy state of the system display more interesting phenomena.

To describe the characteristics of the zero-energy states, we introduce the inverse participation rate (IPR) to analyze the wavefunction locality in more detail. According to previous work [56,57], the IPR is defined as

$$\mathrm{IPR}_n = \frac{\sum_l |\psi_n(l)|^4}{(\sum_l |\psi_n(l)|^2)^2}, \tag{18}$$

where ψ_n is the nth right eigenvector of H [56–60], and l is the site index of the considered system. Usually, IPR is used to calculate the localization degree of each state and quantitatively describe the wavefunction localization. The IPR_n of the localized states tends to be a nonzero and finite value with the increase of the system's size L. It has been found that $\mathrm{IPR}_n \to 1.0$ for completely localized states [58–60]. We then calculate the IPR_n values of the zero-energy states and the isolated states in Fig. 7. For the case of $\delta = -0.7$, IPR_n of four purely imaginary states is equal to $\mathrm{IPR}_{(99\,-\,102)} = 0.8894$, whereas for the bulk states $\mathrm{IPR}_n \to 0$. When $\delta = -0.32$, imaginary-energy states appear in the band gap which are caused by the isolated states precipitated from the bulk states and two purely real zero-energy states. The IPR_n of these are $\mathrm{IPR}_{(99\,-\,102)} = 0.1161$ and $\mathrm{IPR}_{98(103)} = 0.044$. In the case of $\delta = -0.23$, the IPR_n of the zero-energy states is $\mathrm{IPR}_{100(101)} = 0.081$ and the isolated states are $\mathrm{IPR}_{102,\,103(98,\,99)} = 0.048$. By comparing the values of IPR, we can find that the IPR_n of isolated states in Fig. 7(b),(c) decreases from 0.1161 to 0.048. It means that the localization of isolated states in Fig. 7(c) is relatively weaker than the localization of zero-energy modes generated by the isolated states in Fig. 7(b). This result is consistent with the conclusion above. Finally, for $\delta = 0.32$, the IPR_n of twofold-degenerate zero-energy states is $\mathrm{IPR}_{100(101)} = 0.043$. Therefore, the localization of each region can also be clearly displayed by the value of IPR_n.

In the following, we discuss the influence of the imaginary-potential strength γ on the band structure in different regions, as shown in Fig. 8. To be explicit, Fig. 8(a),(b) corresponds to $\delta = -0.4$, Fig 8(c),(d) corresponds to $\delta = -0.2$, and Fig. 8(e),(f) corresponds to $\delta = 0.4$. They de-

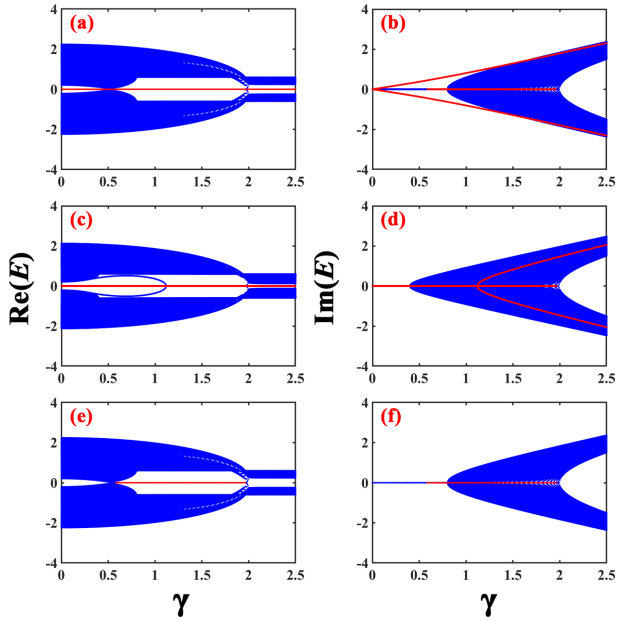

Fig. 8. Real and imaginary parts of energy for different γ. The parameters are (a),(b) $\delta = -0.4$, (c),(d) $\delta = -0.2$, and (e),(f) $\delta = 0.4$. The left panels show the real part of the energy, and the right panels correspond to the imaginary part. Other parameters are $\lambda = 0.3$. The red lines describe the real and imaginary parts of the zero-energy states, respectively.

scribe the topologically nontrivial and topologically trivial regions of the fourfold and twofold degeneracy, respectively. From Fig. 8(a),(b), it can be found that the bulk-state energies for $\gamma < 2\delta t = 0.8$ are real, while those for $\gamma > 0.8$ have imaginary parts. For the zero-energy states, as long as γ is not equal to zero, their energies immediately present imaginary parts, resulting in the system always showing $\mathcal{PT}$- symmetry breaking. Also, between the two topological phase transition points $\sqrt{7}/2 < \gamma < 1.986$, the imaginary potentials drive the emergence of new purely real zero-energy states. When $\gamma > 1.986$, the topological phase transition driven by imaginary potentials is broken, and the purely real zero-energy states disappear. In the case of $\delta = -0.2$ [Fig. 8(c),(d)], when $\gamma < 0.4$, the whole system is of $\mathcal{PT}$ symmetry. When $\gamma > 0.4$, $\mathcal{PT}$-symmetry breaking occurs due to the imaginary part of the bulk-state energies. In addition, with the increase of γ, it can be seen that twofold-degenerate isolated states are indeed precipitated from the bulk states. Due to the zero-energy states generated by the isolated states, the mixed six-state region appears after $\gamma > 1.4$. Until the second topological phase transition, the zero energy of the system changes to a fourfold purely imaginary energy state. Finally, for the case of $\delta = 0.4$, as shown in Fig. 8(c),(d), the system undergoes a $\mathcal{PT}$ phase transition, that is, $\mathcal{PT}$-symmetry breaking occurs at $\gamma > 0.8$. Additionally, it can be found that there is a twofold topological zero-energy state in the gap between the two topological phase transitions. Based on the above results, it can be found that for different types of topological phases in the Hermitian case, the imaginary potentials have different effects on the zero-energy and the bulk states.

Figure 9 shows the effect of λ on energy bands in different regions for the case of $\gamma = \sqrt{7}/5$. Relevant parameters are consistent with Fig. 8. It can be observed that λ can also regulate the energy spectra of the system. For example, in Fig. 9(a),(b), when $\lambda = 0.5$ the bulk states are split from the two-band to four-band structure, and four purely imaginary energy states will appear

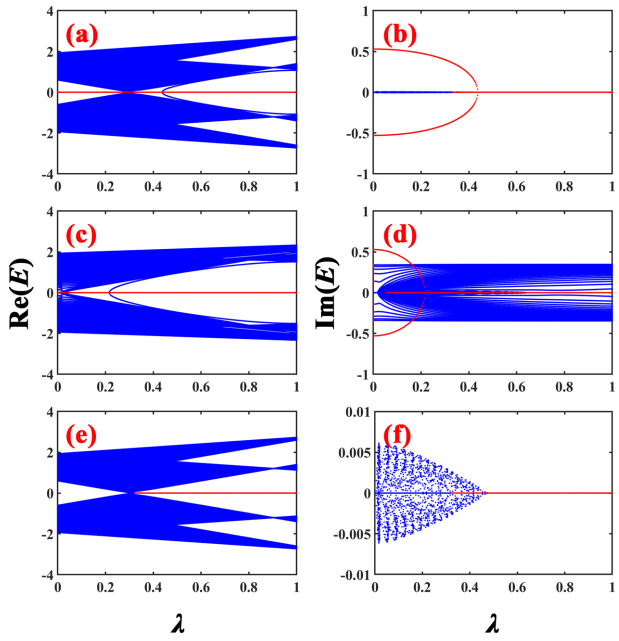

Fig. 9. Real and imaginary parts of energy for different λ. The parameters are (a),(b) $\delta = -0.4$, (c),(d) $\delta = -0.2$, and (e),(f) $\delta = 0.4$. The left panels show the real part of the energy, and the right panels correspond to the imaginary part. Other parameters are $\gamma = \sqrt{7}/5$. The red lines describe the real and imaginary parts of zero-energy states, respectively.

before the critical value of topological phase transition, $\lambda = 0.3$. Then a mixed six-state region appears, and isolated states appear in the band gap. If $\delta = -0.2$, the change trend of zero-energy states is similar to those in Fig. 9(a),(b), except that the bulk states have imaginary parts in the whole parameter space. The specific results are shown in Fig. 9(c),(d). When $\delta = 0.4$, it can be observed that under the action of imaginary potentials, topological phase transition occurs at $\lambda = 0.3$ and twofold-degenerate zero-energy states appear. Furthermore, the bulk-state bands also split at $\lambda = 0.5$ and become purely imaginary at $0 < \lambda < 0.5$. This shows that the spin–orbit coupling has a special regulatory effect on the energy band and topology of the non-Hermitian 1D spin–orbit-coupled SSH lattice.

Next, we introduce diagonal disorder to observe their variations. Figure 10 shows the energy spectra of the SSH lattice modulated by disorder mechanisms of different strengths, for the cases of $\delta = -0.7$ and $\delta = 0.32$. According to Fig. 7(a),(d), the system has four purely imaginary states when $\delta = -0.7$ and degenerate purely real zero-energy states when $\delta = 0.32$. Figure 10(a)–(d) shows the eigenenergy spectra due to the disorder of onsite potentials with the increase of d. The disorder is considered in the manner of $i\gamma + dg_n$ [61], where d is the disorder strength and g_n is uniformly distributed between -0.5 and 0.5. Figure 10(a),(b) corresponds to the case of $\delta = -0.7$. As shown in Fig. 7(a), where $d = 0$, four purely imaginary states exist in the band gap. Herein, following the enhancement of disorder, the real part of the edge-state energy splits into four, symmetric about the energy-zero point, whereas their imaginary part tends to be independent of the presence of disorder. The splitting of the real part of the energy indicates that the edge states are not robust to disorder. Instead, the bulk-state energies display the opposite variation in this process. The imaginary part of them is found to show nonzero values which are proportional to the enhancement of d.

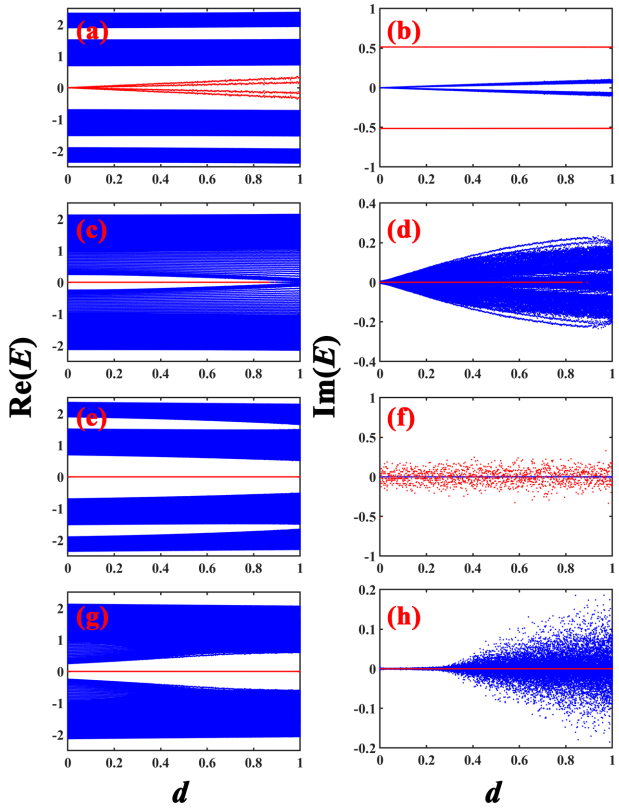

Fig. 10. Energy spectra of the SSH lattice influenced by disorder mechanisms of different strengths. The SSH lattice length is taken to be $N_c = 50$, and the spectra are the average over 100 disorder results. In (a)–(d), the disorder is applied according to the manner of $i\gamma + dg_n$ with $g_n \in [-0.5, 0.5]$ and d being the disorder parameter. (a),(b) Eigenenergy spectra for $\delta = -0.7$; (c),(d) results for $\delta = 0.32$. In (e)–(h), the disorder is applied according to the manner of $i(\gamma + dg_n)$ with $g_n \in [-0.5, 0.5]$. (e),(f) Eigenenergy spectra for $\delta = -0.7$; (g),(h) results for $\delta = 0.32$. Other parameters are taken to be $\gamma = \sqrt{7}/5$ and $\lambda = 0.3$.

The results in Fig. 10(c),(d) describe the case for $\delta = 0.32$. From Fig. 7(d), we know that in the absence of disorder, this system can display degenerate purely real zero-energy states. Next when the strength of disorder d is not equal to zero, we find that in the region of $0 < d < 0.87$, the degenerate purely-real zero-energy states still exist, showing a certain robustness to disorder. For the bulk states, the increase of disorder enhances the imaginary part of the bulk-state energies and narrows the gap of the real part of them. As a result, the increase of the bulk band causes the system gap to decrease, resulting in the entry of the zero-energy state into the bulk state, and causing the zero-energy states to disappear.

For comparison, in Fig. 10(e)–(h) we present the results when the disorder is applied according to the manner of $i(\gamma + dg_n)$ [32], where g_n is also uniformly distributed between -0.5 and 0.5. It can be noticed that in such a case, the imaginary potentials are affected by disorder. One sees in Fig. 10(e),(f) that in the case of $\delta = -0.7$, the disorder only perturbs the imaginary part of the edge-state energies. Alternatively, when $\delta = 0.32$, the gap of the real part of the bulk-state energies is widened by the increase of disorder. Therefore, we find that different types of diagonal disorder have different modification effects on the bulk- and edge-state energy spectra of the system.

3.2 *Transmission assisted by edge states*

To further clarify the properties of the different edge states, we construct a one-compound system with the spin–orbit-coupled SSH chain coupled to two semi-infinite lattices. Our purpose is to present the transmission behaviors of this system assisted by the edge states.

The Hamiltonian of the whole lattice can be written as

$$H = H_c + H_l + H_t. \tag{19}$$

where H_l is the Hamiltonian of the two semi-infinite lattices, which is given by

$$H_l = \sum_{\alpha\in L,R}\sum_{l\sigma} t_0 a^{\dagger}_{\alpha,l\sigma} a^{\dagger}_{\alpha,l+1\sigma} + \text{h.c.}, \tag{20}$$

where $a^{\dagger}_{\alpha,l\sigma}(a_{\alpha l\sigma})$ is an operator to create (annihilate) an particle at site $l\sigma$ in lattice α, $\alpha \in L, R$ represents the Left and right semi-infinite lattice and t_0 is the corresponding intersite hopping energy. The last term in the Hamiltonian denotes the tunneling between the semi-infinite lattices and the SSH chain. Since we assume that the two semi-infinite lattices are coupled to one terminal of the SSH chain, H_t is expressed as

$$H_t = \sum_{\alpha\sigma}\left(\tau_\alpha a^{\dagger}_{\alpha,1\sigma} c_{1a\sigma} + \text{h.c.}\right), \tag{21}$$

where τ_α denotes the chain–lattice coupling coefficient.

Following the Hamiltonian above, the transmission behaviors can be evaluated using the nonequilibrium Green-function technique [62–65]. For our system, the transmission function can be directly expressed as $T(\omega) = \sum_{\sigma\sigma'} T_{\sigma\sigma'}(\omega)$ with

$$T_{\sigma\sigma'}(\omega) = 4\text{Tr}\left[\Gamma^L_\sigma G^r_{\sigma\sigma_1}\Gamma^R_{\sigma_1} G^a_{\sigma_1\sigma'}\right]. \tag{22}$$

Γ^α_σ is the matrix describing the coupling strength between the SSH chain and lattice α. It is defined as $\Gamma^\alpha_\sigma = \pi|\tau_\alpha|^2\rho_0(\omega)$. In Eq. (22), the retarded and advanced Green functions in the Fourier space are involved. These Green functions can be solved by means of the equation-of-motion method. Via a straightforward derivation, the matrix form of the retarded Green function can be written out, that is,

$$G^r = [\omega - H_c - \Sigma_L - \Sigma_R]^{-1} \tag{23}$$

with $\Sigma_\alpha = H_t g_\alpha H_t^{\dagger}$. g_α is the surface Green function of the semi-infinite lattice. In view of the Hamiltonian in Eq. (20), g_α can be expressed directly, that is, $g_\alpha = \frac{\omega - i\sqrt{4t_0^2-\omega^2}}{2t_0^2}$. The advanced Green functions can be expressed as $G^a = (G^r)^{\dagger}$.

Figure 11 shows the spectra of the transmission function for the cases of $\delta = -0.7$, -0.32, 0.32, and 0.7, respectively. Note that since the SSH chain is non-Hermitian, the transmission function is no longer unitary. Accordingly, Fig. 11 shows the normalized transmission function. As shown in Fig. 11(a)–(d), the transmission function exhibits different profiles in the respective cases. To be explicit, when $\delta = -0.7$, one transmission plateau is formed in the region of $|\omega| \leq 0.7$. This result can be attributed to the appearance of the purely imaginary-energy states in the band gap [see Fig. 7(a)]. Such states provide open conditions for the transmission between the two semi-infinite lattices. Thus, no peaks, but only a single plateau, arise in the transmission function spectrum. Next, for the case of $\delta = -0.32$, one peak appears in the transmission function spectrum. This peak exactly corresponds to the real-energy edge states. As shown in Fig. 7(b) two real-energy states are induced in the band gap. Then, their coupling to the semi-infinite lattices produces one channel for quantum transmission. Figure 11(c) also exhibits the transmission peak at $\omega = 0$ which is caused by the presence of real-energy edge states. In this

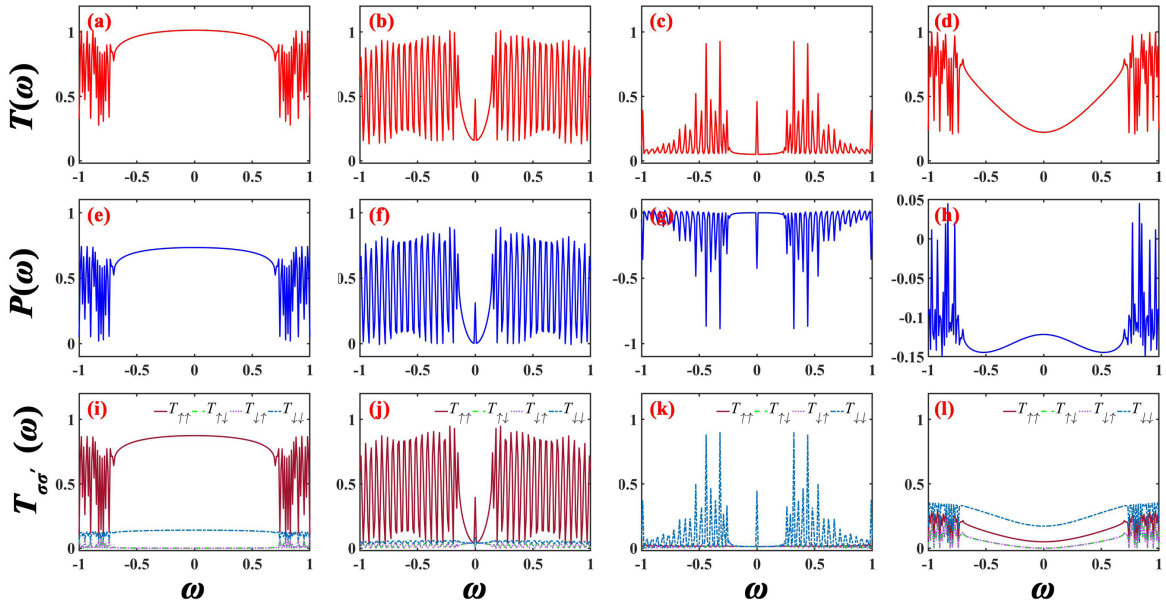

Fig. 11. Transmission function spectra for $\delta = -0.7$, -0.32, 0.32, and 0.7. Other parameters are taken to be $\gamma = \sqrt{7}/5$, $\lambda = 0.4$, and $t = 1$: (a)–(d) show the transmission function curves; (e)–(h) are the corresponding spin transmission results; and (i)–(l) are the respective components of the transmission function.

case, no imaginary-energy edge states exist, so the transmission near $\omega = 0$ is forbidden. On the other hand, in the topologically trivial region, one transmission valley forms due to the absence of any edge states. Therefore, the transmission function spectra can differentiate the influences of the various edge states in an efficient way.

Due to the coexistence of spin-dependent imaginary potentials and spin–orbit coupling, we decided to investigate the spin polarization of the transmission function. To do so, we define the spin transmission as $P(\omega) = \sum_\sigma [T_{\uparrow\sigma} - T_{\downarrow\sigma}]$. The results of spin transmission are shown in Fig. 11(e)–(h). The components of the transmission function are shown in Fig. 11(i)–(l). It can be clearly seen that for $\delta = -0.7$ and -0.32, the spin transmission spectra are almost the same as the transmission function in Fig. 11(a),(b). This undoubtedly means that the spin-up transmission function contributes dominantly to the transmission function [see Fig. 11(i),(j)]. Hence in these cases, high-efficiency spin polarization comes into being. Next, in the case of $\delta = 0.32$, the spin transmission displays the same profile as the transmission function, but its magnitude is negative. One can understand that this result originates from the dominant contribution of the spin-down transmission process [see Fig. 11(k)]. We thus know that in the respective regions, spin polarization properties are different from each other. Alternatively, Fig. 11(h) shows that in the topologically trivial region, the spin polarization is relatively weak. All these results show that in our considered SSH lattice, spin transmission is also an important quantity to describe the edge states induced by the interplay between spin–orbit coupling and imaginary potentials.

4. Summary

We have performed theoretical investigations into the topological and energy properties of a 1D non-Hermitian spin–orbit-coupled SSH lattice by introducing spin-dependent imaginary potentials with gain and loss. As a result, it has been found that imaginary potentials lead to the appearance of imaginary energies in the topologically nontrivial region, and $\mathcal{PT}$ phase transi-

tion occurs in the topologically trivial region. In addition, the imaginary potentials and spin–orbit coupling work together to make the topological phase transition occur in the topologically trivial region, and the topologically nontrivial region is widened. The energy spectrum results show that imaginary potentials and spin–orbit coupling have obvious effects on the zero-energy states of this system, mainly due to the presence of four types of zero-energy states with different localization and numbers. This shows the special adjustment effect of imaginary potentials and spin–orbit coupling on the band structure of such a system. Furthermore, we introduce two forms of diagonal disorder and find that the energy spectra of the bulk and edge states have obvious changes under different types of disorder. This indicates that different topological regions have different regulatory effects on disorder. Next, the properties of the respective topological states have been further described by investigating the transmission behaviors of the SSH lattice. This shows show that the topological states play a nontrivial role in driving the quantum transmission. We believe these results are helpful for describing the topological phase transition behaviors of $\mathcal{PT}$-symmetric non-Hermitian systems with spin–orbit coupling.

Acknowledgments

This work was financially supported by the National Natural Science Foundation of China (Grant No. 11905027), the LiaoNing Revitalization Talents Program (Grant No. XLYC1907033), and the Fundamental Research Funds for the Central Universities (Grant No. N2002005).

REFERENCES

[1] C. M. Bender and S. Boettcher, Phys. Rev. Lett. **80**, 5243 (1998).
[2] G. Q. Liang and Y. D. Chong, Phys. Rev. Lett. **110**, 203904 (2013).
[3] J. M. Zeuner, M. C. Rechtsman, Y. Plotnik, Y. Lumer, S. Nolte, M. S. Rudner, M. Segev, and A. Szameit, Phys. Rev. Lett. **115**, 040402 (2015).
[4] S. Malzard, C. Poli, and H. Schomerus, Phys. Rev. Lett. **115**, 200402 (2015).
[5] R. El-Ganainy, K. G. Makris, M. Khajavikhan, Z. H. Musslimani, S. Rotter, and D. N. Christodoulides, Nat. Phys. **14**, 11 (2018).
[6] X. H. Wang, T. T. Liu, Y. Xiong, and P. Q. Tong, Phys. Rev. A **92**, 012116 (2015).
[7] L. Jin, Phys. Rev. A **97**, 012121 (2018).
[8] S. K. Agarwal and N. Y. Joglekar, Phys. Rev. A **104**, 022218 (2021).
[9] Z. H. Xu, R. Zhang, S. Chen, L. B. Fu, and Y. B. Zhang, Phys. Rev. A **101**, 013635 (2020).
[10] M. S. Rudner and L. S. Levitov, Phys. Rev. Lett. **102**, 065703 (2009).
[11] L. H. Li, Z. H. Xu, and S. Chen, Phys. Rev. B **89**, 085111 (2014).
[12] C. Li, S. Lin, G. Zhang, and Z. Song, Phys. Rev. B **96**, 125418 (2017).
[13] W. P. Su, J. R. Schrieffer, and A. J. Heeger, Phys. Rev. Lett. **42**, 1698 (1979).
[14] L. Wang, M. Troyer, and X. Dai, Phys. Rev. Lett. **111**, 026802 (2013).
[15] M. Leder, C. Grossert, L. Sitta, M. Genske, A. Rosch, and M. Weitz, Nat. Commun. **7**, 13112 (2016).
[16] M. Lohse, C. Schweizer, O. Zilberberg, M. Aidelsburger, and I. Bloch, Nat. Phys. **12**, 350 (2016).
[17] J. K. Asbóth, L. Oroszlány, and A. Pályi, Lect. Notes Phys. **919**, 1 (2016)
[18] B. G. Zhu, R. Lü, and S. Chen, Phys. Rev. A **89**, 062102 (2014).
[19] Y. Xing, L. Qi, J. Cao, D. Y. Wang, C. H. Bai, H. F. Wang, A. D. Zhu, and S. Zhang, Phys. Rev. A **96**, 043810 (2017).
[20] C. Yuce, Phys. Rev. A **97**, 042118 (2018).
[21] F. Dangel, M. Wagner, H. Cartarius, J. Main, and G. Wunner, Phys. Rev. A **98**, 013628 (2018).
[22] K. L. Zhang, P. Wang, G. Zhang, and Z. Song, Phys. Rev. A **98**, 022128 (2018).
[23] S. Lieu, Phys. Rev. B **97**, 045106 (2018).
[24] J. Jin, P. Wang, and Z. Song, Sci. Rep. **7**, 5903 (2017).

[25] X. S. Li, Z. Z. Li, L. L. Zhang, and W. J. Gong, J. Phys.: Condens. Matter **32**, 165437 (2020).
[26] P. Y. Chang, J. S. You, X. D. Wen, and S. S. Ryu, Phys. Rev. Research **2**, 033069 (2020).
[27] K. Kawabata, Y. Ashida, H. Katsura, and M. Ueda, Phys. Rev. B **98**, 085116, (2018).
[28] M. Klett, H. Cartarius, D. Dast, J. Main, and G. Wunner, Phys. Rev. A **95**, 053626 (2017).
[29] L. Jin, Phys. Rev. A **96**, 032103 (2017).
[30] L. L. Zhang, J. R. Li, D. Zhang, T. T. Xu, B. W. Cui, and W. J. Gong, Results Phys. **34**, 105274 (2022).
[31] X. M. Zhao, C. X. Guo, S. P. Kou, L. Zhuang, and W. M. Liu, Phys. Rev. B **104**, 205131 (2021).
[32] C. H. Zhang, L. Sheng, and D. Y. Xing, Phys. Rev. B **103**, 224207 (2021).
[33] A. Guo, G. J. Salamo, D. Duchesne, R. Morandotti, M. Volatier-Ravat, V. Aimez, G. A. Siviloglou, and D. N. Christodoulides, Phys. Rev. Lett. **103**, 093902 (2009).
[34] Z. Lin, H. Ramezani, T. Eichelkraut, T. Kottos, H. Cao, and D. N. Christodoulides, Phys. Rev. Lett. **106**, 213901 (2011).
[35] B. Zhen, C. W. Hsu, Y. C. Igarashi, L. Lu, I. Kaminer, A. Pick, S. L. Chua, J. D. Joannopoulos, and M. Soljačić, Nature **525**, 354 (2015).
[36] S. Q. Xia, D. KALTSAS, and D. H. Song, Science **372**, 72 (2021).
[37] R. Fleury, D. Sounas, and A. Alù, Nat. Commun. **6**, 5905 (2015).
[38] L. Schindler, A. Li, C. M. Zheng, F. M. Ellis, and T. Kottos, Phys. Rev. A **84**, 040101 (2011).
[39] Z. Lin, J. Schindler, F. M. Ellis, and T. Kottos, Phys. Rev. A **85** 050101 (2012).
[40] Y. Liu, Y. Z. Han, and C. S. Liu, Optik **255**, 168727 (2022).
[41] Y. Z. Han, H. Jiang, S. Chen, and C. S. Liu, Phys. E: Low-Dimens. Syst. Nanostruct. **110**, 68 (2019).
[42] H. B. Xue, Z. L. Duan, B. Chen, J. B. Chen, and L. L. Xing, Acta Phys. Sin. **70**, 087301 (2021).
[43] Y. J. Lin, Jiménez-García K, and I. B. Spielman, Nature **471**, 83 (2011).
[44] L. W. Cheuk, A. T. Sommer, Z. Hadzibabic, T. Yefsah, W. S. Bakr, and M. WZwierlein, Phys. Rev. Lett. **109**, 095302 (2012).
[45] V. Galitski and I. B. Spielman, Nature **494**, 49 (2013).
[46] C. E. Whittaker, E. Cancellieri, P. M. Walker, B. Royall, E. T. L. Rodriguez, E. Clarke, D. M. Whittaker, H. Schomerus, M. S. Skolnick, and D. N. Krizhanovskii, Phys. Rev. B **99**, 081402(R) (2019).
[47] P. St-Jean, V. Goblot, E. Galopin, A. LematreOzawa T et al. Nat. Photonics **11**, 651 (2017).
[48] K. Kawabata, K. Shiozaki, M. Ueda, and M. Sato, Phys. Rev. X **9**, 041015 (2019).
[49] A. Altland and M. R. Zirnbauer, Phys. Rev. B **55**, 1142 (1997).
[50] E. J. Bergholtz, J. C. Budich, and F. K. Kunst, Rev. Mod. Phys. **93**, 015005 (2021).
[51] H. C. Wu, L. Jin, and Z. Song, Phys. Rev. B **103**, 235110 (2021).
[52] K Takata and M. Notomi, Phys. Rev. Lett. **121**, 213902 (2018).
[53] C. H. Wu, N. Liu, G. Chen, and S. T. Jia, Phys. Rev. A **106**, 012211 (2022).
[54] X. D. Zhao, Y. Xing, L. Qi, S. T. Liu, S. Zhang, and H. F. Wang, New. J. Phys. **23**, 073043 (2021).
[55] J. R. Li, L. L. Zhang, W. B. Cui, and W. J. Gong, Phys. Rev. Research **4**, 023009 (2022).
[56] C. X. Guo, C. H. Liu, X. M. Zhao, Y. Liu, and S. Chen, Phys. Rev. Lett. **127**, 116801 (2021).
[57] Q. Lin, T. Y. Li, L. Xiao, K. K. Wang, W. Yi, and P. Xue, Phys. Rev. Lett. **129**, 113601 (2022).
[58] Y. X. Liu, Y. C. Wang, X. J. Liu, Q. Zhou, and S. Chen, Phys. Rev. B **103**, 014203 (2021).
[59] L. J. Zhai and G. Y. Huang and S Yin, Phys. Rev. B **104**, 014202 (2021).
[60] M. C. Cristian and M. I. Molina, Phys. Rev. A **91**, 033815 (2015).
[61] C. Mejía-Corteś and M. I. Molina, Phys. Rew. A **91**, 033815 (2015).
[62] Y. Meir and N. S. Wingreen, Phys. Rev. Lett. **68**, 2512 (1992).
[63] A. P. Jauho, N. S. Wingreen, and Y. Meir, Phys. Rev. B **50**, 5528 (1994).
[64] W. J. Gong, X. Y. Sui, Y. Wang, G. D. Yu, and X. H. Chen, Nanoscale Res. Lett. **8**, 330 (2013).
[65] W. J. Gong, S. F. Zhang, Z. C. Li, G. Yi, and Y. S. Zheng, Phys. Rev. B **89**, 245413 (2014).